Radiation Physics and Chemistry 177 (2020) 109062

Contents lists available at ScienceDirect

Radiation Physics and Chemistry

journal homepage: www.elsevier.com/locate/radphyschem

Evaluation of a Commercial Off The Shelf CMOS Image Sensor for X-ray spectroscopy up to 24.9 keV

Martín Pérez[a,b,c,*], Miguel Sofo Haro[a,b,c], José Lipovetzky[a,b,c,d], Andres Cicuttin[e], María Liz Crespo[e], Fabricio Alcade Bessia[a,c,d], Mariano Gómez Berisso[a,c,d], Juan Jerónimo Blostein[a,c,d]

[a] Centro Atómico Bariloche and Instituto Balseiro, Av. E. Bustillo 9500, R8402AGP, San Carlos de Bariloche, Rio Negro, Argentina
[b] Comisión Nacional de Energía Atómica (CNEA), Argentina
[c] Universidad Nacional de Cuyo (UNCUYO), Argentina
[d] Consejo Nacional de Investigaciones Cientficas y Técnicas (CONICET), Argentina
[e] The Abdus Salam International Centre for Theoretical Physics (ICTP), Strada Costiera 11, Trieste, Italy

ARTICLE INFO

Keywords:
CMOS
Image sensors
X-rays
Spectroscopy

ABSTRACT

We studied the X-ray spectroscopy capability and the detection efficiency of a low cost Commercial Off The Shelf CMOS Image Sensor (CIS) in the energy range from 6.4 to 24.9 keV using the fluorescence spectra emitted by FeNi, Cu, Zr, Pb, and Ag. The obtained results are compared with that obtained using a Silicon Drift Detector (SDD). We conclude that CIS is able to resolve fluorescence lines up to 17.7 keV but with a reduced detection efficiency. At lower energies, the energy resolution of the CIS is comparable to that obtained with the SDD. By the comparison of both detectors we also estimate the detection efficiency of the proposed method and the effective thickness of the CIS for all the measured X-ray lines.
2010 MSC: 00-01, 99-00.

1. Introduction

Since their discovery at the end of the eighteenth century, X-rays have been used for diagnosis and non destructive test in several applications related with science, medicine, and industry (Allen, 1931). The use of X-rays in radiography and diffractometry can provide information about the structure and properties of samples under study. X-ray spectroscopy has applications in many disciplines including engineering, archaeology, astronomy, health, conservation, restoration of cultural heritage, etc. Semiconductors detectors like: Si-PIN diodes, germanium detectors, and silicon drift detectors (SDDs) are widely used in X-ray spectroscopy due to many advantages such as, reduced size, high energy resolution and high efficiency (Sharma, 2012). Hybrid Pixelated detectors with spectroscopic capabilities allow the acquisition of X-ray transmission energy selective images (Procz et al., 2010, Procz et al., 2009); the acquisition of fluorescence X-rays images (Uher et al., 2011), and even improve the quality of diffraction data in materials analysis (Ponchut and Zontone, 2003).

Monolithic pixelated sensors fabricated in Complementary Metal Oxide Semiconductor (CMOS) technologies have been used in many applications for ionizing radiation detection (Perić, 2007, Perić et al., 2013). In particular, several works have shown that low cost Commercial Off The Shelf (COTS) CMOS Image Sensors (CIS), designed and fabricated to capture visible light images in consumer electronic products, can also be used as ionizing radiation detectors. Their use as sensors for personal and environmental dosimetry has been proposed previously (Magalotti et al., 2014, Pérez et al., 2016, Shoulong et al., 2017). Yan et al. (2020) show that with adequate image processing it is possible to use the images of a CIS from an uncovered surveillance camera to detect ionizing radiation in an environmental detector. Moreover, Cucuic (Cuciuc, 2018) has proven that although with a low efficiency, it is possible to detect muons generated by cosmic rays in the atmosphere using CMOS image sensors. In (Pérez et al., 2016) we have shown that it is possible to classify different particles detected by the CIS based on the amount of charge and geometrical parameters of the cluster of pixels of each interaction. This classification method was used in (Bessia et al., 2018) to explain the damage caused by thermal neutrons in CIS containing boron in the pre-metal insulator layers.

In reference (Pérez et al., 2018) we present a sensitive thermal neutron detection technique, based on a CIS covered with a gadolinium conversion layer. Reference (Alcalde Bessia et al., 2018) proves that it is possible to obtain Xray images with high spatial resolution by using

* Corresponding author. Centro Atómico Bariloche and Instituto Balseiro, Av. E. Bustillo 9500, R8402AGP, San Carlos de Bariloche, Rio Negro, Argentina.
E-mail address: martin.perez@ib.edu.ar (M. Pérez).

https://doi.org/10.1016/j.radphyschem.2020.109062
Received 13 February 2020; Received in revised form 30 April 2020; Accepted 15 June 2020
Available online 02 August 2020
0969-806X/

Commercial Off The Shelf CMOS image sensors (Lipovetzky et al., 2020), shows the use of CIS to the acquisition of false color radiographs using data from different energy ranges and brightnesses.

On the other hand, it was demonstrated that Commercial Off The Shelf CMOS image sensors can be used to perform X-ray spectroscopy. The article (Lane, 2012) examines the use of low cost CMOS sensors for X-ray imaging and spectroscopy, the work (Hoidn and Seidler, 2015) shows the integration of a CIS and a single-board computer into an X-ray camera platform for acquisition of spectra and radiographs in a range of energies of 26 keV.

CIS have a smaller pixel pitch compared to hybrid detectors (Jungmann et al., 2011), and would allow the same applications with better spatial resolution. On the other side, compared to other hybrid pixelated detectors and SDD, the low dark current and noise per pixel allow the use of the sensor at room temperature, simplifying its use in portable or low cost systems.

In (Haro et al., 2019), we performed low energy X-ray spectroscopy employing a CIS model MT9M001 manufactured by ON Semiconductor (On semiconductor MT9M001, 2019). In that work (Haro et al., 2019), we also introduced the configuration and the processing techniques that were used to measure X-ray energies in the range from 1 to 10 keV. In order to improve the energy resolution of the CIS, the measurements presented in (Haro et al., 2019) were carried out by setting the gain of all the pixels of the sensor at its maximum value (15 ×). Due to this gain setting, it was not possible to measure the energy of photons of more than 10 keV, because there was a saturation of the Analog to Digital Converter (ADC) of the sensor. In (Pérez et al., 2020) we explored other gain values in order to do spectroscopy with X-rays of more than 10 keV, and we also probe that it is possible to resolve X-ray lines up to 17.6 keV using a gain of 4 × without a significant degradation in the energy resolution. In this work we measured the fluorescence spectra of FeNi, Cu, Zr, Pb and Ag, to analyze the interval of energies in which it is possible to employ this technique. We also obtained the spectrum of these materials with a Silicon Drift Detector in order to do a comparison between both detectors and to be able to calculate the efficiency of the CIS in the range of energies of 6.4–24.9 keV.

In Section 2, we will present the experimental details. In Section 3 we will show the fluorescence spectra and the comparison between the resolution obtained with the CIS and the Silicon Drift Detector. In Section 4, we will present the estimation of the detection efficiency of the method, and the estimation of the effective thickness of the CIS for all the measured X-ray lines. Finally, in Section 5 we will present the conclusions of this work.

2. Materials and methods

In this section we will describe the Materials and methods used to obtain the fluorescence spectra presented in this work.

2.1. CMOS image sensor and readout electronics

The integrated circuit used in the measurements is a front side illuminated 1/2-inch monochrome CMOS active-pixel sensor model MT9M001STM manufactured by ON Semiconductor (On semiconductor MT9M001, 2019). This sensor has an active imaging array of 1280×1024 pixels with a pitch of 5.2 μm × 5.2 μm. Fig. 1 shows a cross section of the sensor employed in this work, the image was obtained with a Scanning Electron Microscope and a Focus-Ion Beam. The Si active volume is covered by a 3.7 μm of insulators and metal layers, and an array of organic microlenses with maximum thickness of ~ 1.3 μm. No color filters are present in this black and white sensor. The chip has an internal ADC with a resolution of 10 bits, and a two-wire serial interface bus that can be used to configure several features like: Gain, frame rate, frame size, white balance, etc.

The readout electronics is composed by two boards: A Camera Module that contains a socket where the CMOS sensor is placed, and the

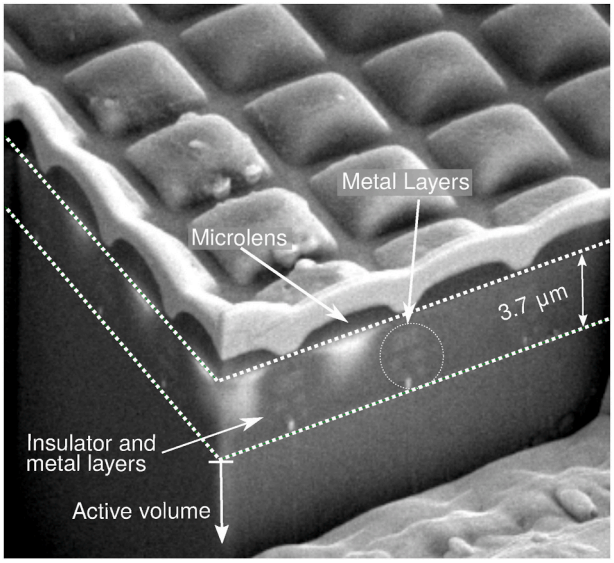

Fig. 1. Cross section of the CIS employed in this work. The image was obtained with a Scanning Electron Microscope and a Focus-Ion Beam microscope. The active volume of the CIS is covered with a 3.7 μm of insulators and metal layers. Over the layer of insulators it is possible to observe the cross sections of the array of microlenses employed to focus the light in the sensitive area of the pixels. The microlenses are made of organic materials and have a maximum thickness of ~ 1.3 μm. It can be seen that the metal layers of the chip do not cover the area below the microlenses —which is the active area of the pixels—. The image also shows the metal layer deposited over the surface of the microlenses which is employed to obtain the image with the microscope.

Arducam Camera Shield that uses an FPGA to read the sensor and transfer the obtained images to a computer via USB (Arducam, 2019). The communication between the *Arducam* Camera Shield and the PC is done using a Python script which collects the image data produced by the sensor. The script also configures the acquisition parameters.

The manufacturer of the chips recommends some gain settings that offers superior noise performance. In this case, the CIS was configured with a gain of 4 × to extend the energy range of the method up to 17 keV (Pérez et al., 2020). The shutter width was set in order to have a pixel integration time of 6.3 ms.

The automatic black level calibration module of the sensor changes the offset of the pixel values according to the average intensity of 256 pixels from two dark rows of the chip (On semiconductor MT9M001, 2019). The pixels of these dark rows are sensible to the X rays, and can produce artifacts in the measurements, therefore the automatic black level calibration was disabled.

2.2. Silicon drift detector

In order to validate and compare the results, we also employed a Silicon Drift Detector *Amptek X-123SDD* to measure the fluorescence spectra of the different materials (AMPTEK Inc, 2019). This Silicon Drift Detector has an active area of 25 mm^2 and a thickness of 500 μm. Its surface is covered with an Amptek C1 window to block visible light (AMPTEK Inc, 2019). The comparison between the spectra obtained with both techniques allows to estimate the detection efficiency of the presented method. The *X-123SDD* was biased with a voltage of −261 V, and its thermoelectric cooler was set to work at a temperature of 221 K. The measurements were done with a peaking time of 2.4 µs, a flat top width of 0.1 µs, and a gain of 4 ×.

2.3. Experimental setup

The X-ray photons necessary to study the performance of the CIS

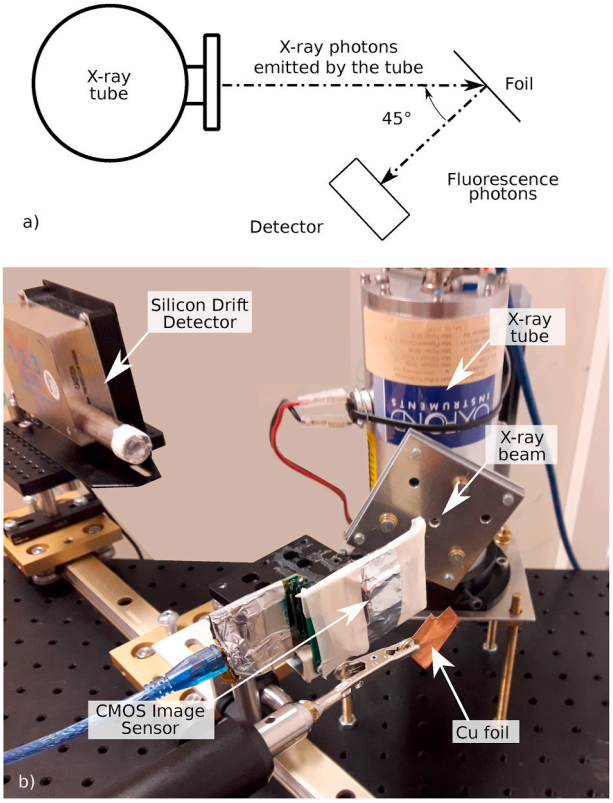

Fig. 2. a) Scheme of the experimental setup used to obtain the X-ray spectra. b) Image of the experimental setup, it is possible to observe the X-ray tube, and the position of a cooper foil. The image also shows the CIS and the SDD mounted on the rail.

were produced by the fluorescence of FeNi, Cu, Zn, Pb and Ag foils. These materials were chosen because their characteristic X-ray lines are spread in the range of energies under study. In order to obtain the spectra, the foils were irradiated with photons generated by an *OXFORD Jupiter 5000 Series* X-ray shielded tube with a palladium target. This X-ray source can be powered with voltages up to 50 kV, and has a spot size of about 50 μm. The voltage of the tube was adjusted in each measurement in order to emit photons with enough energy to produce the fluorescence of the foils. On the other hand, the current was set at its maximum value—1 mA—to obtain the highest X-ray flux.

Fig. 2 a shows a scheme of the experimental setup. The fluorescent target materials were placed in front of the X-ray beam at a distance of 10 cm of the tube, and with an angle of 45° with respect to the beam axis. The surface of the CIS was placed parallel to the foils at a distance of 3 cm. In this configuration the sensor receives the fluorescence photons and is not directly exposed to the main beam.

The detectors were mounted on a rail, which was set normal to the analyzed fluorescent beam, as shown in Fig. 2 b, allowing to exchange and place them at the exact same position with respect to the foils every time. The surface of the CIS was covered with an aluminium tape of 130 μm thick to avoid the interaction between the visible light and the pixels of the sensor.

3. Results

In this section we will present the fluorescence spectra obtained after processing the acquired data. In previous works (Haro et al., 2019, Pérez et al., 2020) we described the detailed procedure to reduce the noise of the images generated by the CIS, and the techniques to extract the events produced by the photons. The first step of the processing is to remove the noise of the analyzed image. We employ an auto regressive

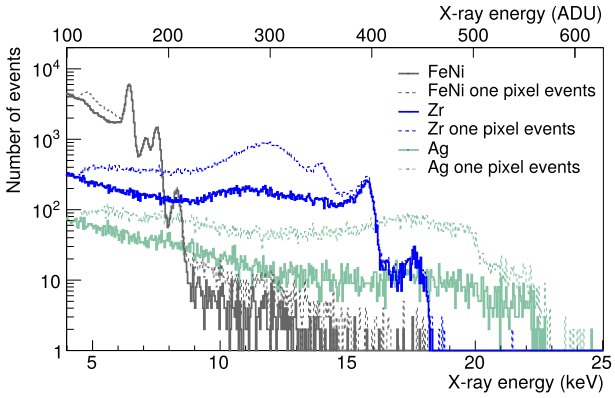

Fig. 3. Fluorescence spectra obtained with foils of FeNi—black curve—, Zr —blue curve— and Ag—green curve—. The curves represented with dashed lines were obtained taking into account all the registered events, while the plots represented with continuous lines where obtained only with one-pixel events.

filter that uses the previous fifteen images to calculate the baseline of the pixels, then these values are subtracted to the processed frame. The processing of the acquired images was done with a custom C++ code, and the analysis of the spectra was performed using the ROOT data analysis framework (Brun and Rademakers, 1997).

When a ionizing particle interacts with the sensor loses energy generating ionization charge on a cluster of pixels, which can be observed as an illuminated region in the image (Pérez et al., 2016). To acquire the spectra, we consider that the ionizing events generated by X-rays are recorded as clusters of pixels whose amplitudes are greater than four times the noise fluctuation, which has a Gaussian distribution with a mean value of zero and a standard deviation of 77 eV (Pérez et al., 2020).

Fig. 3 shows the fluorescence spectra of FeNi—Fe61/Ni39 alloy—, Zr and Ag, the K_α lines of Fe—6.399 keV—and the K_β lines of Ag—25.00 keV—are at the ends of the analyzed energy range[1] (Kaye et al., 1960). The curves represented with dashed lines depict the spectra obtained taking into account all the detected events. On the other hand, the curves plotted using continuous lines represents the spectra obtained considering only one-pixel events in which the ionization charge has been collected only by a single pixel.

In (Haro et al., 2019) we presented the Incomplete Charge Collection phenomenon (ICC), and we proved that the loss of charge in the inter-pixel volumes impairs the energy resolution of the method. We also showed that it is possible to improve the resolution taking into account only one-pixel events in which the losses of charge are less preponderant. As it will be detailed in Section 4.2, the fluorescence peaks produced by the FeNi foil are in the range of 6.39–8.26 keV, due to the low energies of these X-rays the majority of these events—in the range between 150 to 220 ADU—affects only one pixel of the CIS, thus allowing to resolve the X-ray lines of the spectrum. On the other hand, mostly of the events generated by the K_α and K_β lines of the Ag—that have energies of 22.12 and 25.00 keV respectively—are composed by clusters of several pixels. Due to the ICC it is not possible to resolve the fluorescence lines in this range of energies which can be seen in the curves presented in Fig. 3. In the case of the K_α line of Zr, it is possible to observe that the peak obtained with one-pixel events is narrower than the acquired considering all the registered events. Therefore, it can be seen that it is possible to achieve a better energy resolution taking into account only the one-pixel events, which is consistent with the results presented in (Haro et al., 2019).

Fig. 4 shows the spectra obtained with FeNi, Cu, Pb, Zr, and Ag fois.

[1] In all of the cases, when the peaks are composed by more than one X-ray line, the energy employed to perform the calculations presented in this work is the average of all these lines weighted by their intensity.

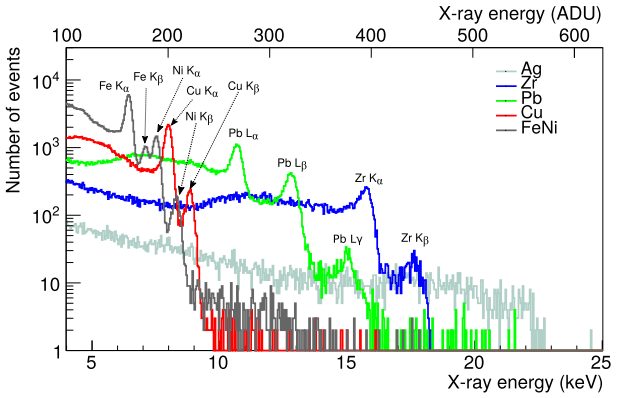

Fig. 4. Fluorescence spectra produced with foils of FeNi, Cu, Pb, Zr, and Ag. All the plots were generated taking into account only one-pixel events.

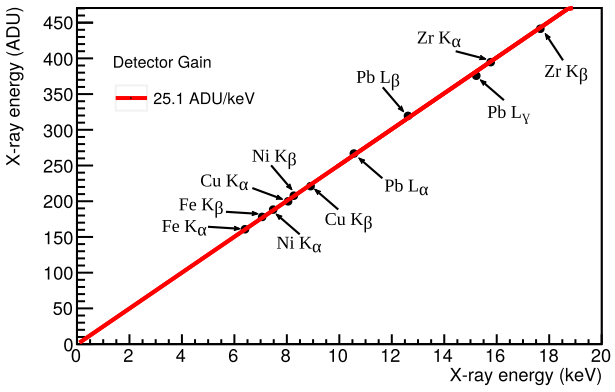

Fig. 5. Energy calibration of the CIS. The resulting gain of the sensor is 25.1 ADU/keV. It is not possible to observe the experimental uncertainties of the dots because in all cases they are smaller than the symbol size.

All plots were generated taking into account only one-pixel events. As a consequence of the reduction in the pixel gain to 4 × it is possible to extend the energy range presented in (Haro et al., 2019). With this configuration the CIS can resolve more energetic peaks as the K_α and K_β lines of 15.74 and 17.70 keV produced by Zr, and the L_α, L_β and L_γ lines—10.54, 12.57 and 14.84 keV respectively—produced by Pb.[2]

Fig. 5 shows the calibration curve of the sensor, the values of energy expressed in ADU were obtained fitting all of the measured peaks with Gaussian functions and estimating their mean values. It is possible to observe that the response of the CIS is linear in this energy range. The slope of the curve represents the energy gain of the sensor and, in this case, the obtained value is 25.1 ADU/keV.

The energy gain of the CIS was used to perform an energy calibration of the spectra formerly presented in Fig. 4. Fig. 6 presents the spectra measured with the CIS—the x-axis units were transformed according to the energy calibration—and the SDD. By the comparison of both plots it can be observed that in the case of the CIS, the relative amplitudes of the peaks fall as the energy increases, this is produced by the reduction in the detection efficiency. Taking into account the results presented in Fig. 6, it is possible to observe that the energy limit for this particular sensor —front side illuminated with a pixel pitch of 5.2 μm—configured with this gain value is between 17.7 and 20 keV.

Due to the high detection efficiency of the SDD, there is a high counting rate at a distance of 3 cm from the foils. In order to avoid pile up and to reduce dead time, the spectra presented in Fig. 6 were measured at a distance of 25 cm from the foils, and normalized to obtain the flux of photons at the CIS position.

In the spectra obtained with the SDD it can be seen the K_α and K_β lines of the Ag that cannot be detected with the CIS. The SDD also can resolve the lines L_l and $L_{\gamma 3}$ of Pb that have energies of 9.185 keV and 15.222 keV respectively. In the Ag and Pb spectra it is also possible to observe the K_α line of Pd—21.178 keV—emitted by the tube that reaches the surface of the SDD after Bragg diffraction in the foils.

Table 1 presents the width of all the measured X-ray lines. These values were obtained by fitting the peaks with Gaussian functions and calculating its standard deviation (σ). The table also shows the ratio between the sigma of the peaks measured with the SSD and the CIS. Observing this relation, it is possible to see that the energy resolution of the Silicon Drift Detector is between 15 and 75% better than the resolution of the CIS.

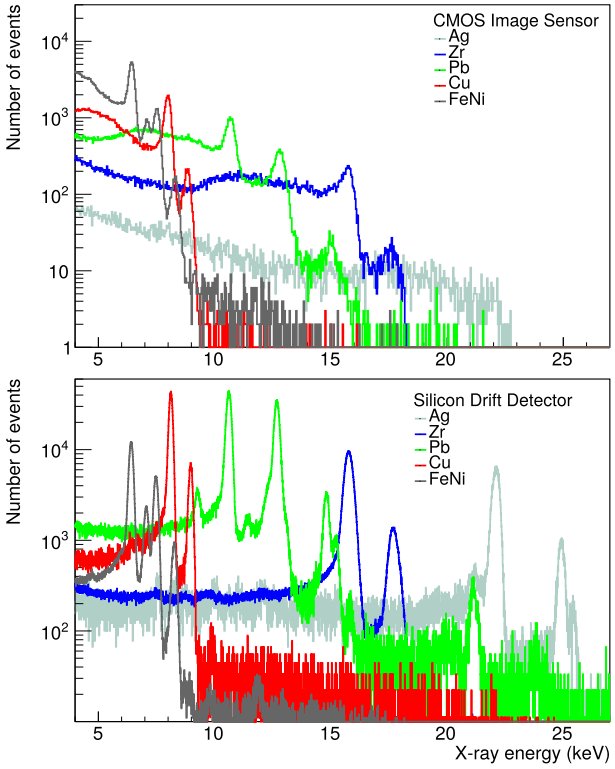

Fig. 6. Comparison between the spectra obtained with the CIS (top) and the SDD (bottom). The vertical axis presents the number of events per channel. The measurement with the CIS lasted 13 min and the measurement with the SDD took 10 min.

4. Discussion

In this section we will present an estimation for the detection efficiency of the presented method. We will also estimate the effective thickness of the sensor for all the energy range employing different models. In all the cases will describe the procedure to obtain the presented values.

4.1. Detection efficiency

The detection efficiency $\eta_m(E)$ is a function of the X-rays energy E and can be obtained with the formula:

$$\eta_m(E) = \frac{N_{CIS}(E)}{\varphi(E)\, t_{adq}\, A_{CIS}} \quad (1)$$

[2] In the spectrum of Pb, the L_α peak is produced by the lines $L_{\alpha 1}$ and $L_{\alpha 2}$ 10.55 and 10.45 keV respectively, the L_β peak is produced by the lines $L_{\beta 1}$, $L_{\beta 2}$, $L_{\beta 3}$, and $L_{\beta 4}$, of 12.61, 12.62, 12.79 and 12.30 keV respectively, finally the L_γ peak is produced by the lines $L_{\gamma 1}$ and $L_{\gamma 3}$ of 14.76 and 15.22 keV respectively.

Table 1
Width of the peaks measured with the CIS and the Silicon Drift Detector expressed in eV. The presented values were obtained fitting a Gaussian function to the peaks and obtaining its standard deviation (σ). The last column shows the ratio between the widths measured with the CIS and the SDD.

Peak	Energy (keV)	σ_{CIS} (eV)	σ_{SDD} (eV)	$\sigma_{SDD}/\sigma_{CIS}$
Fe K_α	6.399	139 ± 1	97 ± 1	0.70
Fe K_β	7.058	221 ± 9	116 ± 2	0.53
Ni K_α	7.472	140 ± 3	95 ± 1	0.68
Cu K_α	8.041	149 ± 1	78 ± 2	0.53
Ni K_β	8.265	166 ± 12	105 ± 1	0.63
Cu K_β	8.904	154 ± 5	87 ± 1	0.57
Pb L_α	10.544	333 ± 4	107 ± 1	0.32
Pb L_β	12.574	320 ± 5	114 ± 1	0.36
Pb L_γ	14.844	511 ± 30	126 ± 2	0.25
Zr K_α	15.744	233 ± 9	185 ± 1	0.79
Zr K_β	17.701	239 ± 46	203 ± 2	0.85

The values of $N_{CIS}(E)$ were obtained calculating the sum of the events in each peak of the spectra measured with the CIS. We performed the efficiency calculation taking into account two sets of $N_{CIS}(E)$ values: The first set was obtained considering the spectra showed in Fig. 4 in which we take into account only one-pixel events where the charge sharing with neighboring pixels is less preponderant (Haro et al., 2019). The second set was obtained employing the spectra generated with all registered events, in which the total amount of counts in each peak is the highest, but the energy resolution is degraded due to the ICC. The factor $\varphi(E)$ represents the flux of photons with energy E that reach the active area of the CMOS sensor. These values were obtained from the measurements made with the SDD and are expressed in photons per cm^2 and second. Each value of $\varphi(E)$ was obtained summing all the events of each peak of the curves presented in Fig. 6, taking in account the area, live time and dependence on E of the SDD detection efficiency (Detector efficiency faq, 2014). The parameter t_{adq} is the time employed by the CIS to acquire the total amount of images necessary to generate the spectra—in this case all the spectra were generated with 5000 images. Finally, A_{CIS} is the active area of the CIS (35.43 mm^2).

The square dots presented in Fig. 7, show the values of $\eta_m(E)$ obtained only with the one-pixel events spectra. On the other hand, the rhomboidal dots of the plot shows the efficiency calculated taking into account all the registered events. As can be seen in Fig. 3 for lower energies −6 to 8.9 keV— most of the events that make up the peaks affects only one pixel of the CIS, thus the efficiency is the same for both cases. The detection efficiency is approximately 5.5% for the lowest energy peak of 6.399 keV. Otherwise, for energies greater than 10 keV the one-pixel events are a fraction of the total count of each peak, therefore the efficiencies obtained taking into account the single-pixel events are lower than the calculated with all the events. At the highest energy (17.7 keV) the efficiency calculated taking into account one-pixel events falls to ~ 0.12% and the value obtained with all the events falls to ~ 0.13%.

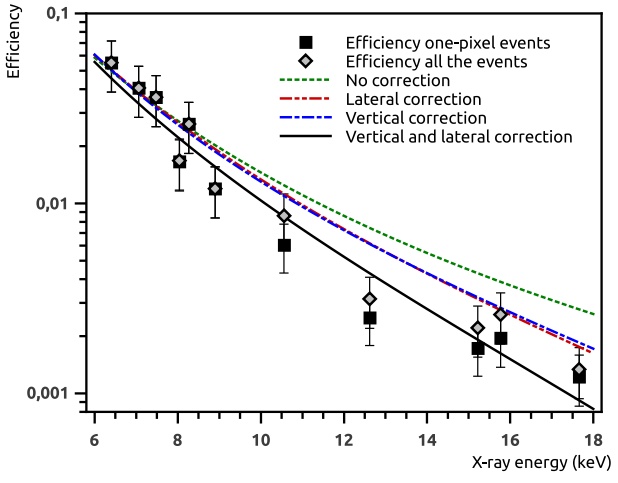

Fig. 7. Square dots: detection efficiencies of the CIS calculated taking into account only one-pixel events. Rhomboidal dots: detection efficiencies computed with all the registered events. Green curve: theoretical efficiency for an effective thickness of 2 μm. Blue curve: theoretical efficiency weighted by the difference between the effective thickness of the sensor and the radius of the ionization cloud—vertical correction—. Red curve: theoretical efficiency weighted by the inter-pixel charge-sharing probability—lateral correction—. Black curve: theoretical efficiency weighted by the lateral and vertical corrections.

4.2. Effective thickness

In order to estimate the effective thickness of the CIS ($t_{EFF-CIS}$) in the measured range of energies, we employed the method presented in (Detector efficiency faq, 2014)—which is used by the manufacturer of the SDD to compute its detection efficiency—. This method employs the total attenuation coefficients for the layers placed in front of the active volume—taking into account its composition and thicknesses— to calculate the scattering and absorption probabilities. The detection efficiency can be estimated using the equation:

$$\eta(E) = \left(e^{(-\mu_1(E)\,\delta_1 t_1 - \ldots - \mu_N(E)\,\delta_N t_N)}\right)\cdot\left(1 - e^{-\mu_{CIS}\,\delta_{Si}\,t_{EFF-CIS}}\right) \quad (2)$$

The first factor of the Equation (2) represents the transmission probability through the layers that cover the active volume of the CIS which in this case are the aluminum layer used to block the visible light, and SiO_2 interlayer dielectrics which cover the center of the pixel. The attenuation of the X-rays in the microlens is negligible compared to all other experimental uncertainties and can be disregarded (Alcalde Bessia et al., 2018). The result of the interaction between the layers that cover the active volume of the CIS and the X-rays is an exponential attenuation of the beam. The interaction processes in the microlenses and the metal layers can be characterized by a probability of occurrence per unit path length. The constants μ_i are the total attenuation coefficients of the materials of each layer expressed in cm^2/g, δ_i are the densities of the materials expressed in g/cm^3, and t_i are thicknesses of each layer. The total probability of absorption of the photon can be obtained by the sum of the probabilities for the individual processes. The second term of the Equation (2) represents the interaction probability into the active volume of the detector and can be calculated as the probability of not transmission in the active volume (Detector efficiency faq, 2014).

At lower energies, the measured efficiency is consistent with an effective thickness between 1.8 and 2.6 μm. Overlaped with the measured efficiencies of Fig. 7, we plot the theoretical efficiencies for a $t_{EFF-CIS}$ of 2 μm—green curve. In previous works (Alcalde Bessia et al., 2018) the depletion thickness of the P-N junction of the device was estimated to be of ~ 1 μm. In (Haro et al., 2019) it was concluded that the effective thickness for one-pixel charge collection is close to ~ 2 μm, taking in account that charge generated in the quasi neutral region close to a P-N junction can be collected by diffusion. This value is comparable or slightly smaller than the typical thicknesses of Si epitaxial layers in these CMOS technologies, which are in the order of approximately 3 to 12 μm depending on the fabrication process (Virmontois et al., 2016) (Lee et al., 2003) (Lalucaa et al., 2013).

As energy increases, the theoretical efficiency is higher than the values calculated with the measured data. This apparent reduction in the detection volume can be explained taking into account the effect of the radius of the ionization cloud and the lateral dimension of the pixels. The linear range in Si of electrons (R_e–) generated by photons can be estimated with the Equation presented in (Everhart and Hoff, 1971):

$$R_e^-(\mu m) = 0.0171 E_e^{1.75} \quad (3)$$

NIST (Berger et al., 1998) also provides an estimation of the electron linear ranges, slightly smaller than Equation (3). However, due to multiple scattering process, it is accepted that electrons leave in average most of their charge in a radius four times smaller than the linear range (Yousef).

For photo-electrons of 6.4 keV, R_{e^-} is approximately 0.44 μm, with most of the charge spread in a radius of a tenth of a micron (Yousef). Since this radius is smaller than the lateral and depth dimensions of the active pixel region, most of the electrons of this energy generate all the ionization charge in the volume of the pixels. The detection efficiency for low energies in Fig. 2 is consistent with an effective thickness of ~ 2 μm.

However, as the energy of the photo-electrons increases, their range in Si is higher. For instance, the range of the photo-electrons generated by photons of 17.6 keV is approximately 2.6 μm. This means that most of the ionization charge will be deposited in a larger charge cloud, with a radius comparable to the sensitive layer thickness.

4.3. Vertical correction

If ionization does not occur completely within the active volume of the sensor, the recorded event will not be part of the analyzed peak, thus for higher energies the measured efficiencies are lower than the computed theoretically. Therefore, is necessary to use a new model to contemplate this phenomenon and perform a vertical correction. The theoretical efficiency presented in the blue curve of Fig. 7 was calculated with the model:

$$\eta_{vc}(E) = \left(e^{(-\mu_1(E)\,\delta_1 t_1 - \ldots - \mu_N(E)\,\delta_N t_N)}\right)\cdot\left(1 - e^{-\mu_{CIS}\,\delta_{Si}\,(t_{EFF-CIS}-R_{e^-})}\right) \quad (4)$$

In this case the efficiency is computed taking into account the difference between the effective thickness of the sensor and the radius of the ionization cloud. This model contemplates the reduction of the efficiency produced by particles that left a fraction of their charge in the active volume of the pixels. The curve obtained employing this model is consistent with the efficiencies calculated taking into account all the registered events.

4.4. Lateral sharing correction

In the case of the efficiency calculated with one-pixel events also is necessary to take into account the lateral dimensions of the pixels, and the inter-pixel charge-sharing probability in order to weight the theoretical efficiency by the probability to have a single-pixel event (horizontal correction). The red curve of Fig. 7 presents the theoretical efficiency weighted by the inter-pixel charge sharing probability (p_{sh}). The model employed to calculate this probability was presented in (Iniewski et al., 2007):

$$p_{sh} = 1 - \frac{(a + 2c2r)^2}{(a + g)^2} \quad (5)$$

Where a is the pixel pitch (5.2 μm), c is an adjustment constant, r is the radius of the electron cloud and g is the inter-pixel gap (~0.52 μm). The black curve presented in Fig. 7 presents the theoretical efficiency calculated taking into account the relation between the effective thickness and the radius of the ionization cloud (vertical correction) and the inter-pixel charge sharing probability (lateral correction). This curve is consistent with the efficiency obtained with one-pixel events in which there is no inter-pixel charge sharing.

5. Conclusions

We employed a Commercial of the Shelf CMOS sensor to perform spectroscopy of X-rays with energies between 6.4 and 17.7 keV. We observed that the response of the CIS is linear in this range of energies and we obtained a detector gain of 25.1 ADU/keV. Due to the Incomplete Charge Collection phenomenon this kind of sensor could not resolve fluorescence lines of more than 20 keV like the K_α and K_β lines of the Ag. We compared the response of the CIS with a Silicon Drift Detector. It can be seen that the CIS was able to resolve the majority of the X-ray lines present in the measured energy range. We also observed that the energy resolution of the Silicon Drift detector is between 15 and 75% better than the resolution of the CMOS sensor.

The detection efficiency of the sensor using single-pixel events ranges from approximately 5.5% for 6.4 keV to 0.12% for 17.7 keV. If the detection efficiency is computed employing all the registered events, it is possible to achieve a better efficiency for X-ray lines of more than 10 keV at the expense of a degradation in the energy resolution. The reduction of the detection efficiency —in the range of 10 to 17.7 keV— is caused by particles that left a fraction of their generated charge in the sensitive layer of the pixels, thus producing events that are not part of the analyzed peak. In the case of the efficiencies obtained with one-pixel events there is also a reduction in the efficiency produced by the inter-pixel charge sharing. It is worth to notice that the results presented in this aricle are only valid for the CIS here analyzed —ON Semiconductor model MT9M001STM— which has a pixel pitch of 5.2 micrometers. The performance of other CIS to carry out X-ray spectroscopy will depend on the characteristics of the employed device, especially the active pixel volume, and pixel pitch.

The CIS analyzed in this work is specially useful for the acquisition of high spatial resolution X-ray images selecting different energy ranges, can be used at room temperature and do not require a complex readout electronics or cooling systems like CCD devices. Thus, employing this technology it is possible to develop low cost detectors with a high spatial resolution, that can be used for multiespectral X-ray imaging, beam characterization, portable spectrometers, etc.

CRediT authorship contribution statement

Martín Pérez: Investigation, Writing - original draft, Writing - review & editing, Visualization, Investigation. **Miguel Sofo Haro:** Investigation, Formal analysis, Writing - review & editing. **José Lipovetzky:** Investigation, Formal analysis, Funding acquisition, Writing - review & editing, Supervision. **Andres Cicuttin:** Investigation, Resources, Funding acquisition, Writing - review & editing. **María Liz Crespo:** Resources, Funding acquisition. **Fabricio Alcade Bessia:** Software, Investigation, Writing - review & editing. **Mariano Gómez Berisso:** Resources, Funding acquisition. **Juan Jerónimo Blostein:** Investigation, Formal analysis, Funding acquisition, Writing - original draft, Writing - review & editing, Methodology, Supervision.

Declaration of competing interest

The authors declare that they have no known competing financial interests or personal relationships that could have appeared to influence the work reported in this paper.

Acknowledgments

This work was supported by ANPCyT (Argentina) under projects PICT 2014-1966 and PICT 2015-1644, and by SIIP Universidad Nacional de Cuyo (Argentina) under projects C036 and C553. The authors would like to thank to Ignacio Artola, Werner Florian, Luis Guillermo García Ordoñez, and Bruno Valinoti for their help during the irradiations and to all of the ICTP Multidisciplinary Laboratory Staff.

References

Alcalde Bessia, F., Pérez, M., Lipovetzky, J., Piunno, N.A., Mateos, H., Sidelnik, I., Blostein, J.J., Sofo Haro, M., Gómez Berisso, M., 2018. X-ray micrographic imaging system based on COTS CMOS sensors. Int. J. Circ. Theor. Appl. 46 (10), 1848–1857.

Allen, H., 1931. X-rays and their applications. Nature 127 (3201), 356.
Arducam, 2019. http://www.arducam.com/arducam-usb-camera-shield-released accessed: 2018-12-5.
Berger, M.J., Coursey, J., Zucker, M., Chang, J., et al., 1998. Stopping-power and Range Tables for Electrons, Protons, and Helium Ions. NIST Physics Laboratory, Gaithersburg, MD.
Bessia, F.A., Pérez, M., Haro, M.S., Sidelnik, I., Blostein, J.J., Suárez, S., Péreza, P., Berisso, M.G., Lipovetzky, J., 2018. Displacement damage in CMOS image sensors after thermal neutron irradiation. IEEE Trans. Nucl. Sci.
Brun, R., Rademakers, F., 1997. Rootan object oriented data analysis framework. Nucl. Instrum. Methods Phys. Res. Sect. A Accel. Spectrom. Detect. Assoc. Equip. 389 (1–2), 81–86.
Cuciuc, M., 2018. Suitability of the raspberry pi camera for cosmic ray detection and measurement. In: 2018 IEEE Nuclear Science Symposium and Medical Imaging Conference Proceedings (NSS/MIC). IEEE, pp. 1–3.
Detector Efficiency Faq, Ametek Materials Analysis Division., https://www.amptek.com/-/media/ametekamptek/documents/products/efficiency.zip, accessed: 2019-16-12 (2014)..
Everhart, T., Hoff, P., 1971. Determination of kilovolt electron energy dissipation vs penetration distance in solid materials. J. Appl. Phys. 42 (13), 5837–5846.
Haro, M.S., Bessia, F.A., Pérez, M., Blostein, J.J., Balmaceda, D.F., Berisso, M.G., Lipovetzky, J., 2019. Soft X-rays spectroscopy with a commercial CMOS image sensor at room temperature. Radiat. Phys. Chem 108354.
Hoidn, O.R., Seidler, G.T., 2015. Note: a disposable X-ray camera based on mass produced complementary metal-oxide-semiconductor sensors and single-board computers. Rev. Sci. Instrum. 86 (8), 086107.
AMPTEK Inc. Silicon Drift Detectors (SDD) X-123SDD, https://www.amptek.com/-/media/ametekamptek/documents/products/sdd.pdf, accessed: 2019-21-10 (2019)..
Iniewski, K., Chen, H., Bindley, G., Kuvvetli, I., Budtz-Jorgensen, C., 2007. Modeling charge-sharing effects in pixellated czt detectors. In: 2007 IEEE Nuclear Science Symposium Conference Record, vol. 6. IEEE, pp. 4608–4611.
Jungmann, J.H., MacAleese, L., Buijs, R., Giskes, F., De Snaijer, A., Visser, J., Visschers, J., Vrakking, M.J., Heeren, R.M., 2011. Fast, high resolution mass spectrometry imaging using a medipix pixelated detector. J. Am. Soc. Mass Spectrom. 21 (12), 2023–2030.
Kaye, G.W.C., Laby, T.H., Feather, N., Barrell, H., Coulson, E., Scott, J., Öpik, E., 1960. Tables of physical and chemical constants, and some mathematical functions. Phys. Today 13, 56.
Lalucaa, V., Goiffon, V., Magnan, P., Rolland, G., Petit, S., 2013. Single-event effects in cmos image sensors. IEEE Trans. Nucl. Sci. 60 (4), 2494–2502.
Lane, D.W., 2012. X-ray imaging and spectroscopy using low cost COTS CMOS sensors. Nucl. Instrum. Methods Phys. Res. Sect. B Beam Interact. Mater. Atoms 284, 29–32.
Lee, J.S., Hornsey, R.I., Renshaw, D., 2003. Analysis of cmos photodiodes. i. quantum efficiency. IEEE Trans. Electron. Dev. 50 (5), 1233–1238.
Lipovetzky, J., Cicuttin, A., Crespo, M.L., Haro, M.S., Bessia, F.A., Pérez, M., Berisso, M.G., 2020. Multi-spectral X-ray transmission imaging using a BSI CMOS image sensor. Radiat. Phys. Chem.
Magalotti, D., Bissi, L., Conti, E., Paolucci, M., Placidi, P., Scorzoni, A., Servoli, L., 2014. Performance of cmos imager as sensing element for a real-time active pixel dosimeter for interventional radiology procedures. J. Instrum. 9, C01036 01.
On semiconductor MT9M001 https://www.onsemi.com/products/sensors/image-sensors-processors/image-sensors/mt9m001 accessed: 2019-09-30 (2019).
Pérez, M., Lipovetzky, J., Haro, M.S., Sidelnik, I., Blostein, J.J., Bessia, F.A., Berisso, M.G., 2016. Particle detection and classification using commercial off the shelf CMOS image sensors. Nucl. Instrum. Methods Phys. Res. Sect. A Accel. Spectrom. Detect. Assoc. Equip. 827, 171–180.
Pérez, M., Blostein, J.J., Bessia, F.A., Tartaglione, A., Sidelnik, I., Haro, M.S., Suárez, S., Gimenez, M.L., Berisso, M.G., Lipovetzky, J., 2018. Thermal neutron detector based on COTS CMOS imagers and a conversion layer containing gadolinium. Nucl. Instrum. Methods Phys. Res. Sect. A Accel. Spectrom. Detect. Assoc. Equip. 893, 157–163.
Pérez, M., Haro, M.S., Blostein, J.J., Cicutin, A., Crespo, M.L., Bessia, F.A., Berisso, M.G., Lipovetzky, J., February 2020. X-ray spectroscopy up to 17.6 keV using a commercial off the shelf CMOS image sensor. In: Accepted in Argentine Conference in Electronics. CAE 2020, Buenso Aires.
Perić, I., 2007. A novel monolithic pixelated particle detector implemented in high-voltage cmos technology. Nucl. Instrum. Methods Phys. Res. Sect. A Accel. Spectrom. Detect. Assoc. Equip. 582 (3), 876–885.
Perić, I., Fischer, P., Kreidl, C., Nguyen, H.H., Augustin, H., Berger, N., Kiehn, M., Perrevoort, A.-K., Schöning, A., Wiedner, D., et al., 2013. High-voltage pixel detectors in commercial cmos technologies for atlas, clic and mu3e experiments. Nucl. Instrum. Methods Phys. Res. Sect. A Accel. Spectrom. Detect. Assoc. Equip. 731, 131–136.
Ponchut, C., Zontone, F., 2003. Evaluation of medipix-1 in x-ray scattering and x-ray diffraction applications. Nucl. Instrum. Methods Phys. Res. Sect. A Accel. Spectrom. Detect. Assoc. Equip. 510 (1–2), 29–34.
Procz, S., Lubke, J., Zwerger, A., Mix, M., Fiederle, M., 2009. Optimization of medipix-2 threshold masks for spectroscopic x-ray imaging. IEEE Trans. Nucl. Sci. 56 (4), 1795–1799.
Procz, S., Lübke, J., Zwerger, A., Fauler, A., Pichotka, M., Mix, M., Fiederle, M., 2010. Energy selective x-ray imaging with medipix. In: IEEE Nuclear Science Symposium & Medical Imaging Conference. IEEE, pp. 3846–3851.
Sharma, S.K., 2012. X-ray Spectroscopy. BoD–Books on Demand.
Shoulong, X., Shuliang, Z., Youjun, H., 2017. γ-ray detection using commercial off-the-shelf cmos and ccd image sensors. IEEE Sensor. J. 17 (20), 6599–6604.
Uher, J., Harvey, G., Jakubek, J., 2011. X-ray fluorescence imaging with the medipix2 single-photon counting detector. IEEE Trans. Nucl. Sci. 59 (1), 54–61.
Virmontois, C., Durnez, C., Estribeau, M., Cervantes, P., Avon, B., Goiffon, V., Magnan, P., Materne, A., Bardoux, A., 2016. Radiation effects in pinned photodiode cmos image sensors: variation of epitaxial layer thickness. IEEE Trans. Nucl. Sci. 64 (1), 38–44.
Yan, Z., Wei, Q., Huang, G., Hu, Y., Zhang, Z., Dai, T., 2020. Nuclear Radiation Detection Based on Uncovered Cmos Camera under Dynamic Scene, Nuclear Instruments and Methods in Physics Research Section A: Accelerators. Spectrometers, Detectors and Associated Equipment, pp. 163383.
H. Yousef, Energy Dependent Charge Spread Function in a Dedicated Synchrotron Beam Pnccd Detector.